drones

MDPI

Article

A Plant-Level Survival Modeling Framework for Spatiotemporal Strawberry Canopy Decline Using UAV Multispectral Time Series

Jon R. Detka [1,*], Adam J. Purdy [1,2], Forrest S. Melton [2], Oleg Daugovish [3], Christopher A. Greer [4] and Frank N. Martin [5]

1 Department of Applied Environmental Science, California State University, Monterey Bay, Seaside, CA 93955, USA
2 NASA Ames Research Center—Moffett Field, Mountain View, CA 94035, USA
3 University of California Cooperative Extension, Ventura County, Ventura, CA 93003, USA
4 University of California Cooperative Extension, San Luis Obispo County, San Luis Obispo, CA 93401, USA
5 U.S. Department of Agriculture, Agricultural Research Service (USDA-ARS), Salinas, CA 93905, USA; frank.martin@usda.gov
* Correspondence: jdetka@csumb.edu

Highlights

What are the main findings?

- UAV multispectral time series combined with survival modeling enabled plant-level, time-to-event mapping of canopy decline in commercial strawberry fields.
- The Random Survival Forest framework consistently ranked plants by future canopy decline risk across heterogeneous field conditions.

What is the implication of the main finding?

- The approach provides a spatiotemporal risk stratification tool to support targeted field scouting and management decisions.
- Framing repeated UAV observations as a time-to-event process extends drone-based crop monitoring beyond static, single-date stress classification.

Abstract

Timely identification of canopy decline in commercial strawberry production is challenging because visual scouting often misses subtle or spatially heterogeneous symptoms. We developed a plant-level UAV-based monitoring framework that integrates repeated multispectral imagery, canopy-derived metrics, unsupervised clustering, and Random Survival Forest (RSF) time-to-event modeling. The framework was applied across three commercial strawberry fields in Oxnard, California using nine UAV surveys collected from December 2022 to June 2023, yielding 159,220 plant-level monitoring units. NDRE- and Redness Index-based classifications quantified proportional and absolute canopy dieback within standardized hexagonal units and supported survival-based modeling of canopy decline progression. Across withheld test plants from all survey dates, overall concordance indices ranged from 0.88 to 0.95 across fields, indicating strong ability to rank plants by time-to-decline risk under heterogeneous field conditions. Spatial risk maps revealed localized high-risk clusters that expanded over time in fields with greater canopy deterioration, while fields with minimal visible decline exhibited diffuse but stable risk distributions. Post-hoc comparison with operational fumigation rates (280, 336, and 392 kg Pic-Clor 60/ha) showed no consistent association with predicted canopy decline risk. These results demonstrate that framing repeated UAV observations as a time-to-event process enables fine-scale spatiotemporal modeling of canopy decline dynamics and supports risk stratification for targeted field monitoring in commercial strawberry systems.

Academic Editors: Jerzy Chojnacki, Simone Pascuzzi and Marcin Siłuch

Received: 5 February 2026
Revised: 14 March 2026
Accepted: 17 March 2026
Published: 25 March 2026

Keywords: strawberry production; canopy health; machine learning; multispectral imaging; random survival forest; risk analysis; uncrewed aerial system (UAS)

1. Introduction

Strawberries are one of the most widely cultivated fruit crops worldwide, grown in more than 70 countries across multiple continents [1]. In the United States, California produces nearly 90% of the national crop and ranks among the top strawberry-producing regions globally [2,3]. As of 2023, the crop contributed approximately $2.97 billion in farmgate value across 40,285 acres in California [2,4].

Soilborne crown and root rot diseases remain among the most persistent and economically damaging challenges in California strawberry production [5,6]. The primary pathogens include *Macrophomina phaseolina*, *Fusarium oxysporum* f. sp. *fragariae*, *Verticillium dahliae*, and *Phytophthora cactorum* [7]. Aboveground symptoms typically emerge only after substantial root or vascular damage has occurred, making early detection and long-term management difficult [8]. Growers rely on pre-plant soil fumigation of entire fields, a strategy that can be effective but imposes additional cost, logistical constraints, and increasing regulatory scrutiny [9]. Current monitoring practices, including in-season ground scouting and end-of-season assessments, primarily document disease after extensive visible canopy damage has occurred and provide limited spatial or temporal resolution for guiding timely in-season management decisions [10].

Recent advances in remote sensing and statistical modeling offer promising tools for monitoring plant health at field scales relevant to disease management [11,12]. Uncrewed aerial vehicles (UAVs), or drones, enable frequent, field-scale collection of high-resolution imagery, allowing for repeatable monitoring of plant canopy condition throughout the growing season. When equipped with multispectral or hyperspectral sensors, imagery generated from UAVs can detect subtle changes in canopy vigor that may signal physiological stress well before visible symptoms appear [13–15]. Onboard sensors capture spectral patterns that, when paired with ground validation, can be used to infer zones of stress potentially associated with disease or other agronomic factors [16]. While high spatial resolution UAV remote sensing tools are increasingly promoted for early disease detection, imagery captures canopy-level stress responses rather than pathogen presence directly [17]. This distinction highlights the need for analytical frameworks that can interpret repeated canopy observations in a temporally explicit and spatially structured manner.

Vegetation indices such as the Normalized Difference Vegetation Index (Equation (1)), Normalized Difference Red Edge Index (Equation (2)), and Redness Index (Equation (3)) have been shown to correlate with early canopy symptoms and dieback in a range of crops, including strawberry [18,19]. Research has demonstrated that NDRE and NDVI are sensitive to foliar symptoms of *Mycosphaerella fragariae* in strawberry [20]. However, most prior optical and spectral approaches in strawberry have focused on foliar diseases at the leaf level rather than the canopy scale, where visible symptoms such as discoloration or necrosis, and pathogen signs, drive spectral change [21–23]. In contrast, our study explores the use of these indices to detect canopy stress most often associated with soilborne pathogens. In this context, spectral signals are indirect and reflect secondary physiological responses (e.g., stunting, reduced canopy vigor, and dieback) rather than direct pathogen presence. This limitation underscores the importance of integrating canopy-level imagery with spatiotemporal modeling frameworks to track disease progression under real-world field conditions.

Modeling disease progression using canopy metrics in real-world field systems poses several challenges. Stress responses are often nonlinear and influenced by spatial and temporal context, and not all plants exhibit visible decline during the observation window, resulting in censored outcomes. Plants that remain healthy through the final survey contribute right-censored observations, meaning the exact timing of potential decline is unknown. Conventional regression and static classification approaches are not designed to model time-to-event processes with nonlinear trajectories and right-censored outcomes. Framing canopy decline as a time-to-event problem at the plant level provides a natural way to capture progression dynamics and accommodate censored observations. Advances in machine learning have introduced new tools for modeling complex biological processes, including disease development in crops [24,25]. Among these, Random Survival Forest (RSF) provides a powerful, nonparametric framework for time-to-event prediction. RSFs can model nonlinear relationships, handle censored data, and integrate spatiotemporal predictors, making them well suited for analyzing plant-level trajectories of canopy decline under field conditions [26,27].

Here, we evaluate whether repeated UAV-based multispectral observations, integrated within a Random Survival Forest (RSF) time-to-event modeling framework, can model the onset and spatial progression of canopy decline in commercial strawberry fields with persistent *M. phaseolina* pressure. Using data from three commercial fields in Oxnard, California, we assess the ability of plant-level survival models to rank canopy decline risk under heterogeneous field conditions and forward-in-time evaluation. We interpret the results in the context of spatial risk stratification for targeted field monitoring and discuss the implications and limitations of this framework for operational crop management.

2. Methods

The analytical workflow used to derive plant-level canopy decline risk from repeated UAV multispectral imagery is summarized in Figure 1. The framework integrates UAV data acquisition, plant-level feature extraction, survival dataset construction, and Random Survival Forest modeling to generate spatial risk maps of canopy decline.

2.1. Study Site

The study was conducted at a commercial strawberry farm in Oxnard, California. UAV flight surveys focused on 39–40 bed rows across three adjacent fields, each approximately 0.8 ha in size (Figure 2). The fields were planted with the 'Fronteras' strawberry variety, installed in late November 2022, and arranged in bed rows four plants wide. 'Fronteras' is a short-day cultivar developed by the University of California, Davis strawberry breeding program. It is widely grown in California's coastal production regions, particularly Ventura, Santa Barbara, and Monterey counties due to its early fruiting, high yield potential, and firm fruit that is well-suited for commercial packing. The cultivar shows resistance to Fusarium wilt, moderate resistance to Verticillium wilt and Phytophthora root rot, and moderate susceptibility to *M. phaseolina* (California Strawberry Commission, 2024).

Prior to planting, the site was treated with Pic-Clor 60, a pre-plant soil fumigant containing chloropicrin and 1,3-dichloropropene that is widely used in California strawberry production for broad-spectrum suppression of soilborne pathogens. The fumigant was applied before bed formation and sealed with a totally impermeable film (TIF) to enhance fumigant retention and efficacy. The three fields also contained grower-applied pre-plant fumigation blocks with variable rates based on historic disease pressure (Figure 2); these operational treatment zones were incorporated later in a post-hoc analysis to evaluate whether RSF-derived canopy risk differed systematically among fumigation rates.

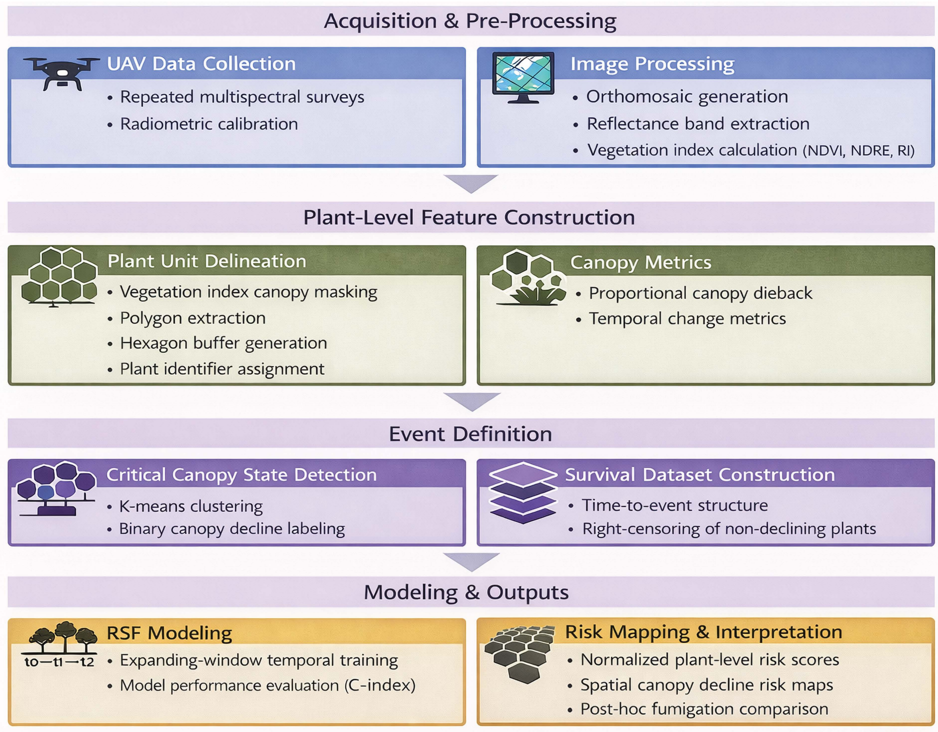

Figure 1. Conceptual workflow for deriving plant-level canopy decline risk from repeated UAV multispectral imagery.

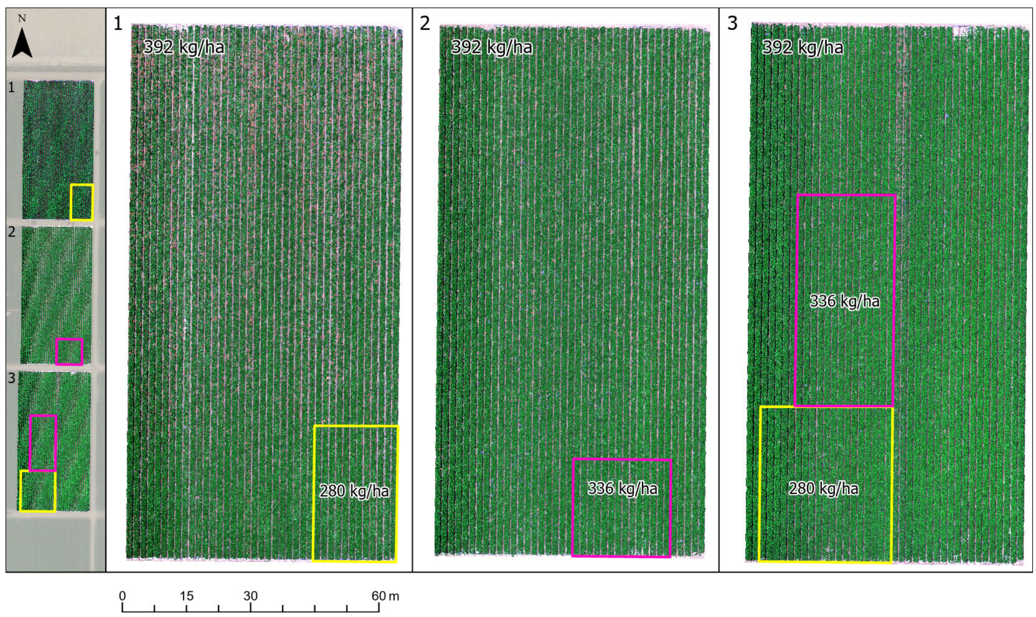

Figure 2. Spatial arrangement of fumigation treatments across the three study fields. Panels (1), (2), and (3) correspond to Fields 1, 2, and 3, respectively. Background shows the 20 June 2023 UAV RGB orthomosaic. Colored outlines indicate variable Pic-Clor 60 soil fumigation rates: yellow = Low 280 kg/ha (250 lbs/acre), magenta = Medium 336 kg/ha (300 lbs/acre). All other areas received the standard rate of 392 kg/ha (350 lbs/acre).

2.2. UAV Data Collection and Imagery Processing

2.2.1. UAV Data Collection

Aerial surveys were conducted using a Matrice 200 V2 quadcopter (Da-Jiang Innovations Sciences and Technologies Ltd. (DJI), Shenzhen, China). Multispectral image data were collected using the MicaSense Altum-PT sensor (EagleNXT, Allen, TX, USA), which measures radiance from five spectral bands (red, green, blue, near-infrared, and red-edge) and a longwave infrared thermal band. To support radiometric correction, the Altum-PT was paired with an irradiance light sensor (Downwelling Light Sensor (DLS 2), EagleNXT, Allen, TX, USA) that recorded sun angle and ambient light conditions during each flight.

To support radiometric calibration, reflectance calibration images were collected using the factory-supplied MicaSense Altum-PT calibration panel (Panel 2, EagleNXT, Allen, TX, USA) prior to each flight. Panel images were used during post-processing to convert raw digital numbers to surface reflectance and, in combination with data from the sensor's downwelling light sensor (DLS 2), to improve radiometric consistency across survey dates. Radiometric calibration has been shown to improve detection consistency in UAV-based plant disease monitoring [28].

Aerial surveys were conducted at 30 m above ground level (AGL) with 85% forward and 75% side overlap with flight speeds below 2 m/s to minimize motion blur. All flights were conducted within one hour of local solar noon to minimize shadow effects and variability in solar illumination. A total of nine drone flights were conducted over three adjacent strawberry fields from December 2022 to June 2023. Flights were spaced approximately nine weeks apart in winter (7 December, 9 February), and 1–3 weeks apart in spring (28 March, 21 April, 15 May, 22 May) and early summer (1 June, 10 June, 20 June).

To ensure accurate georeferencing, seven ground control points (GCPs) were deployed throughout each field. Each GCP consisted of a 0.25 m $\times$ 0.25 m black-and-white checkerboard target. The center of each GCP was surveyed using an REACH RS+ single-band real-time kinematic (RTK) GNSS rover (Emlid Tech Kft., Hungary) connected via an NTRIP correction service, providing horizontal accuracy of approximately $\pm$0.03 m and vertical accuracy of $\pm$0.05 m.

2.2.2. Imagery Processing

Imagery was processed using Pix4Dmapper structure-from-motion photogrammetry software (v4.9.0; Pix4D SA, Lausanne, Switzerland). Each survey yielded approximately 2000 individual images across 5 bands per 1 hectare. Processing followed Pix4D's standard workflow, which includes image alignment, sparse and dense point cloud generation, digital surface model (DSM) creation, and generation of georeferenced orthomosaics and reflectance maps. Ground control points (GCPs) were manually marked across overlapping images to improve georeferencing accuracy.

Image alignment was optimized using Pix4D's agricultural processing settings to improve feature matching in vegetated fields with repetitive textures. Radiometric correction was applied using both the Altum-PT's downwelling light sensor (DLS 2) and reference images of the reflectance calibration target, which was imaged before each flight. These corrections ensured consistent surface reflectance values across survey dates and varying illumination conditions within each flight.

2.3. Plant-Level Canopy Metric Extraction

2.3.1. Feature Extraction and Classification

Post-processed reflectance rasters were analyzed in ArcGIS Pro (v3.3.1; Esri Inc., Redlands, CA, USA) using Python scripts built on the ArcPy library. For each survey date, multispectral composites were clipped by field and vegetation indices were computed from individual band rasters. The indices included the Normalized Difference Vegetation Index (NDVI; [29]) for canopy vigor:

$$\mathrm{NDVI} = \frac{NIR - Red}{NIR + Red} \tag{1}$$

the Normalized Difference Red Edge Index (NDRE; [30]) for early detection of stress in maturing plants:

$$\text{NDRE} = \frac{NIR - RedEdge}{NIR + RedEdge} \tag{2}$$

and a redness index (RI), mathematically equivalent to the normalized green–red difference index (NGRDI; [31]) but with reversed sign, which captures shifts in red and green reflectance associated with senescence or canopy decline:

$$\text{RI} = \frac{R - G}{R + G} \tag{3}$$

NDVI was used to generate binary canopy masks that were converted to polygons and assigned to bed rows via spatial buffering. Polygon centroids were extracted from these canopy objects, deduplicated by proximity, and assigned unique plant-level identifiers for downstream analysis.

Hexagonal buffers (0.17 m radius) were generated around each canopy centroid to standardize the spatial unit of analysis. Within each hexagon, NDRE- and RI-based thresholds (Table 1) were applied using a hierarchical, rule-based classification approach to assign pixels as healthy, dieback, or non-vegetated. NDRE was used to identify vegetated canopy, and RI was subsequently used to refine canopy condition within those areas; pixels not meeting any NDRE or RI threshold were assigned to an unclassified state (0) and excluded from analysis to reduce ambiguity associated with mixed pixels and transitional canopy states. Final canopy class assignments were based on the combined response of both indices rather than independent thresholding.

Table 1. Threshold values for Normalized Difference Red Edge Index (NDRE) and Redness Index (RI) used to classify canopy status. NDRE and RI thresholds were applied hierarchically and include intentional gaps. Pixels not meeting any NDRE or RI range were assigned to an unclassified category (0) and excluded from analysis.

Canopy Class	NDRE Range	RI Range	Interpretation
Healthy	≥0.60	−1.00 to −0.30	Dense, photosynthetically active canopy
Dieback	0.45–0.59	0.22 to 0.37	Thinning or declining canopy; moderate stress
Non-vegetated	0.14–0.41	−0.01 to 0.16	Bare soil, plastic mulch, or senesced vegetation
Unclassified	Outside ranges	Outside ranges	No clear classification; excluded from analysis

These classifications were summarized into plant-level metrics capturing two complementary aspects of canopy decline. Relative dieback was calculated as the proportion of dieback pixels normalized by the total number of vegetated canopy pixels (healthy + dieback) within each hexagon, providing a within-canopy measure of decline severity independent of plant size. In contrast, absolute dieback was calculated as the proportion of dieback pixels relative to all pixels within the hexagon, including non-vegetated background, thereby capturing the total magnitude of canopy loss associated with stunting or reduced canopy extent. Together, these metrics allowed the model to distinguish plants exhibiting severe proportional decline within an otherwise intact canopy from those experiencing larger overall canopy loss. Plant-level canopy metrics were extracted from hexagon buffers representing individual plants, resulting in 159,220 unique plant records with repeated spectral measurements across survey dates (Table 2).

Threshold values for NDRE and RI were selected empirically based on inspection of index value distributions across flights and visual comparison with canopy condition in the orthomosaics. These thresholds were chosen to consistently separate healthy canopy, declining vegetation, and non-vegetated background while conservatively excluding ambiguous pixels at canopy edges. An intermediate unclassified range was intentionally retained to minimize misclassification of mixed pixels between plant canopy and the surrounding soil or furrow. Classification thresholds were held constant across all fields and survey dates to maximize consistency and minimize mixed-pixel artifacts, which was essential for generating stable plant-level metrics used in survival modeling. Because these NDRE and RI threshold values were empirically derived for this dataset using a specific UAV sensor and radiometric processing workflow, they should be considered sensor- and site-specific. Absolute index values may vary across UAV platforms, cultivars, canopy architectures, and environmental conditions. Future work should evaluate adaptive or relative thresholding approaches (e.g., percentile-based classification within fields or dates) to improve transferability across systems while retaining the broader modeling framework.

Table 2. Area and number of plant monitoring units within each fumigation rate class by field. Plant counts represent plant-level hexagon units used in RSF analyses. Total values summarize all fumigation rate classes within each field.

Field	Treatment	Fumigation Rate (kg/ha)	Area (ha)	Plant Count
1	Standard	392	0.733	48,318
	Low	280	0.062	4102
	TOTAL	–	**0.795**	**52,420**
2	Standard	392	0.736	48,830
	Medium	336	0.052	3455
	TOTAL	–	**0.788**	**52,285**
3	Standard	392	0.597	39,478
	Medium	336	0.113	7540
	Low	280	0.112	7497
	TOTAL	–	**0.822**	**54,515**

2.3.2. Critical Cluster Identification

For each UAV survey date, plant-level canopy metrics and their temporal changes were standardized and grouped using k-means clustering ($k = 3$) to identify relative canopy condition states. To prevent information leakage across repeated observations, plants were partitioned into training and test sets before clustering. For each flight date, feature standardization and clustering were fit using training plants only. The cluster exhibiting the highest mean proportional canopy dieback among training plants was designated as the "critical" canopy state. The fitted scaler and cluster centroids were then applied to all plants observed on that flight to assign cluster membership. Plants assigned to the designated critical cluster were labeled as experiencing canopy decline, forming the time-to-event outcome for survival modeling. Distance to the nearest critical plant was explored as a spatial descriptor but was not included in the final RSF models reported here.

2.3.3. Survival Dataset Construction

A survival dataset was created by merging repeated observations for each plant across all flight dates and formatting them into a start–stop interval structure appropriate for time-to-event analysis. The event indicator was defined as whether a plant entered the critical cluster at any flight. Time was computed as the number of days since the plant's first observation, based on the UAV flight calendar. Plants that never entered the critical category during the observation period were treated as right-censored, meaning that the event of interest did not occur before the final survey, and the exact time of potential future decline was unknown.

2.4. Random Survival Forest Modeling

2.4.1. RSF Modeling and Evaluation

Random Survival Forest (RSF) models were implemented in Python using the *scikit-survival* package. Models were fit separately for each field using an expanding-window temporal evaluation design, in which earlier survey dates were used to predict subsequent flights. To prevent information leakage across repeated observations of the same plant, unique plants were randomly partitioned into training (80%) and test (20%) sets using a fixed random seed. All repeated observations for a given plant were confined to a single partition across all dates.

Three independent RSF models were trained, one for each field. The same hyperparameter configuration was used across fields to ensure comparability of model structure. Hyperparameters were selected *a priori* based on preliminary tuning and fixed for all analyses (number of trees = 50, maximum tree depth = 2, minimum samples per split = 40, minimum samples per leaf = 20, and maximum features per split = 2). Fixing hyperparameters across fields isolates performance differences to underlying canopy decline dynamics rather than to field-specific model tuning.

Predictor variables included plant-level canopy metrics capturing proportional dieback and temporal changes in canopy condition. Model performance was evaluated using the concordance index (C-index), which quantifies the ability to correctly rank plants by time-to-decline risk while accounting for right-censoring. Because survival times are identical within individual survey dates, concordance was computed across all withheld test observations spanning multiple flights to ensure meaningful temporal variation. For interpretability at individual survey dates, binary classification metrics (precision, recall, and F1 score) were also computed using thresholded risk scores.

2.4.2. Post-Processing of RSF Risk Scores for Visualization

Continuous RSF-derived risk scores were normalized to a 0–1 scale within each flight to support visualization and temporal summaries. Because normalization was performed independently for each flight, risk classes represent relative risk within a given survey date rather than absolute risk comparable across dates. Temporal changes in canopy condition were, therefore, evaluated using the underlying continuous RSF risk scores and time-to-event structure of the survival model, which preserve information on relative risk accumulation over time. Changes in the proportion and spatial extent of moderate- and high-risk plants across flights reflect the expansion of higher-risk zones rather than direct comparisons of absolute risk magnitude between survey dates. To facilitate visualization, normalized risk scores were discretized into three canopy risk classes based on empirical inspection of risk score distributions across flights. Plants with normalized risk ≤ 0.15 were classified as low risk, those with $0.15 <$ normalized risk ≤ 0.40 as moderate risk, and those with normalized risk > 0.40 as high risk. These categories were used solely for risk maps and percent-at-risk summaries; all statistical analyses and post-hoc treatment comparisons were conducted using continuous RSF risk scores while controlling for field and flight date.

2.4.3. Secondary Classification Analysis

To complement the time-to-event analysis, we also evaluated RSF performance as a per-flight binary classifier. For each test flight, continuous risk scores were thresholded using the value that maximized the F1 score, and plants in the cluster-defined critical group were treated as positive cases. Precision, recall, and F1 scores were computed using the *scikit-learn* package to quantify classification performance across flights. These per-flight classification metrics were intended to support interpretability of risk maps and do not replace survival-based evaluation.

2.5. Post-Hoc Influence of Variable Fumigation Treatment

Because fumigation rates were applied operationally across the study fields based on historical disease pressure, we conducted a post-hoc analysis to evaluate whether RSF-derived canopy risk varied systematically with fumigation intensity.

The study fields were part of a commercial strawberry operation, and pre-plant fumigation treatments were applied operationally rather than as a controlled experiment. Three chloropicrin–1,3-D (Pic-Clor 60) application rates were used across the site (standard = 392 kg/ha; medium = 336 kg/ha; low = 280 kg/ha), arranged in large contiguous blocks selected by the grower based on historical disease pressure and field logistics rather than randomized assignment. As a result, treatment areas were not replicated experimentally, and comparisons represent post-hoc observational patterns rather than causal contrasts.

Fumigation treatment polygons were delineated using field GPS surveys and digitized for spatial analysis. For each UAV survey date, plant-level hexagon units containing RSF-derived risk scores were spatially joined to the fumigation polygons based on spatial overlap. Hexagons intersecting low- or medium-rate polygons were labeled accordingly; all remaining hexagons were assigned to the standard rate category. A summary of fumigation-block areas and associated plant monitoring units within each rate class is provided in (Table 2). These comparisons were intended to explore associations between operational fumigation intensity and modeled canopy decline risk, rather than to infer treatment efficacy.

Within-field treatment effects were evaluated using plant-level normalized RSF-derived canopy risk as the response variable. To address unequal sample sizes among rates, analyses were conducted on balanced subsamples created by random downsampling to equalize the number of plants per available rate within each field. Treatment effects were estimated using linear models with fumigation rate as a fixed effect and flight date included as a covariate, with standard errors clustered by flight date. As a robustness check, mixed-effects models with flight date specified as a random intercept were also fit to evaluate sensitivity of treatment effect estimates to model structure.

3. Results

3.1. Spatial Patterns of Decline

Among the three study fields, Field 1 exhibited the strongest late-season shift toward high canopy risk, with clear spatial expansion of high-risk plants over time (Figure 3). In mid-May, moderate- and high-risk plants were relatively balanced (approximately 4.7% and 3.8%, respectively), but by 1 June the proportion of high-risk plants increased sharply while moderate-risk plants declined. By 10 June, high-risk plants comprised approximately 12% of the field, whereas moderate-risk plants remained below 1%, indicating consolidation of canopy decline into more severe, spatially coherent zones. Spatial maps show early scattered hotspots coalescing into larger contiguous patches, particularly along central and northern regions of the field.

In contrast, Field 2 showed consistently low and spatially diffuse canopy risk without sustained expansion. Moderate-risk plants ranged from approximately 1.5–3.5% across survey dates, while high-risk plants remained below 3% and declined to below 0.5% after 15 May (Figure 4). Risk maps revealed scattered individual plants classified as moderate or high risk at different survey dates, with little temporal persistence at the individual-plant level and no evidence of patch-level coalescence. These patterns indicate limited field-wide canopy decline and a predominantly diffuse stress signal.

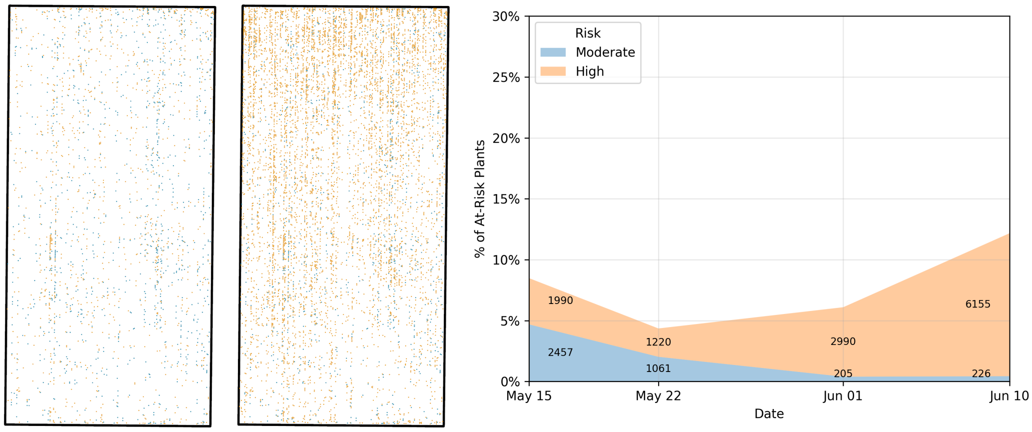

Figure 3. Spatiotemporal patterns of RSF-derived canopy risk in Field 1. Plant-level risk maps illustrate moderate and high canopy risk on 22 May 2023 (**left**) and 10 June 2023 (**right**), with the accompanying time series showing changes in the proportion of at-risk plants across survey dates.

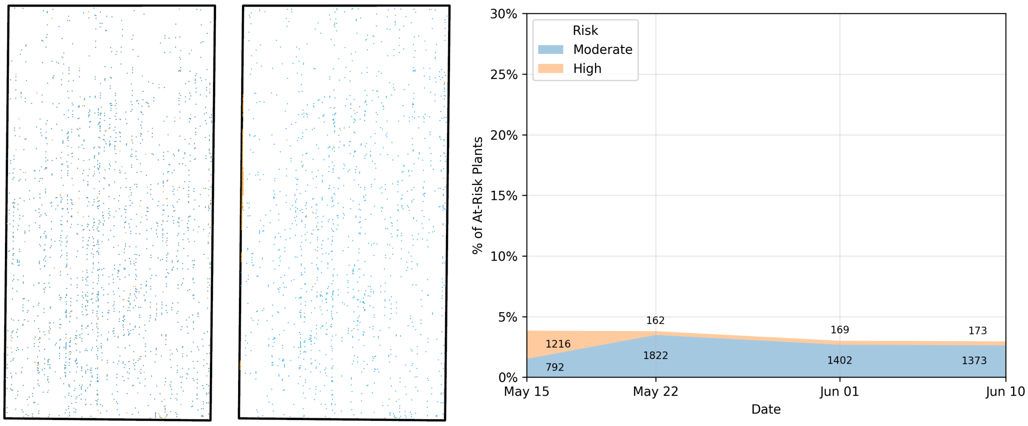

Figure 4. Spatiotemporal patterns of RSF-derived canopy risk in Field 2. Plant-level panels depict survey dates 22 May 2023 (**left**) and 10 June 2023 (**right**) as representative examples. Risk remained spatially diffuse with consistently low proportions of moderate- and high-risk plants across survey dates, as summarized in the accompanying time series.

Field 3 exhibited localized but persistent canopy risk concentrated within a small number of adjacent rows (Figure 5). Moderate-risk plants remained between approximately 1–2% for most of the season before declining in late June, while high-risk plants remained below 3% throughout the observation period. Spatial maps show that elevated risk was largely confined to recurring, spatially coherent zones rather than expanding across the field. These patterns indicate limited overall canopy decline but stable localized areas of elevated stress that were not readily apparent from field-wide visual inspection.

3.2. Random Survival Forest Model Performance

All reported performance metrics reflect out-of-sample evaluation on withheld plants using plant-level splits and temporally forward test flights, ensuring that model performance reflects generalization rather than memorization.

Across the three commercial fields, overall survival ranking performance was consistently strong. Concordance indices computed across pooled test flights were 0.88 for Field 1, 0.92 for Field 2, and 0.95 for Field 3, indicating that RSF models reliably ranked plants by time-to-decline risk under heterogeneous field conditions.

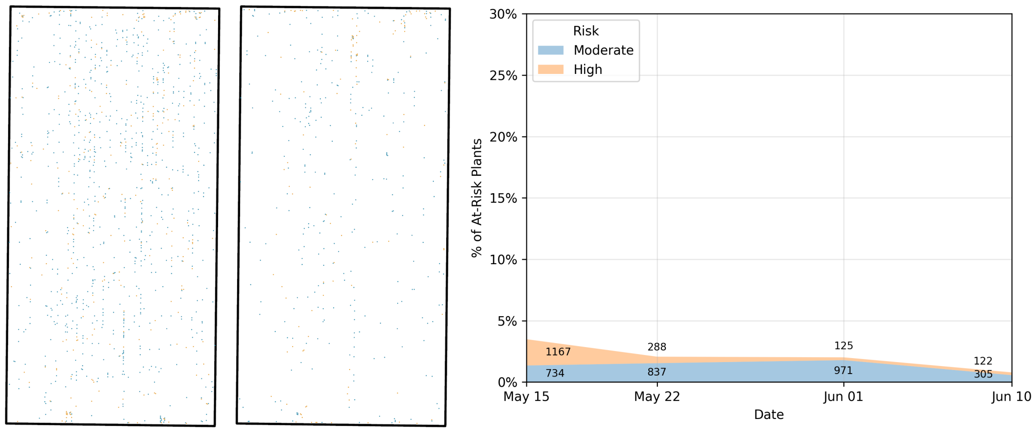

Figure 5. Spatiotemporal patterns of RSF-derived canopy risk in Field 3. Plant-level panels depict survey dates 22 May 2023 (**left**) and 10 June 2023 (**right**) as representative examples. Risk was concentrated in localized zones within the field, while the majority of plants remained low risk throughout the season, as reflected in the accompanying time series.

Per-flight classification performance, summarized using precision, recall, and F1 score (Table 3), varied across fields and survey dates in ways that reflected differences in canopy decline prevalence and spatial coherence. In Field 1, classification performance was highest during periods of spatially coordinated canopy deterioration (e.g., 22 May; F1 = 0.89) but declined late in the season under extreme class imbalance as high-risk plants became more prevalent. In Field 2, where canopy decline remained low and spatially diffuse, classification performance was moderate but relatively stable across flights. In Field 3, where decline was sparse and localized, per-flight F1 scores fluctuated as event prevalence varied, with lower performance during low-incidence flights and stronger performance when localized decline intensified.

Table 3. RSF test performance by field and temporally forward test flight. Precision, recall, and F1 reflect binary classification of canopy decline on withheld plants for each test flight.

Field	Flight	Precision	Recall	F1
Field 1	4/21/2023	0.151	0.430	0.224
	5/15/2023	0.280	0.333	0.304
	5/22/2023	0.830	0.964	0.892
	6/1/2023	0.125	0.019	0.033
	6/10/2023	0.011	0.002	0.004
	6/20/2023	0.017	0.003	0.005
Field 2	4/21/2023	0.932	0.929	0.930
	5/15/2023	0.977	0.712	0.824
	5/22/2023	0.963	0.802	0.875
	6/1/2023	0.805	0.969	0.879
	6/10/2023	0.665	0.872	0.754
	6/20/2023	0.528	0.735	0.615
Field 3	4/21/2023	0.909	0.963	0.935
	5/15/2023	0.902	0.805	0.851
	5/22/2023	0.281	0.351	0.312
	6/1/2023	0.769	0.866	0.815
	6/10/2023	0.826	0.863	0.844
	6/20/2023	0.694	0.721	0.707

Taken together, these results indicate that binary classification accuracy depends strongly on the spatial and temporal structure of canopy decline, whereas survival-based ranking performance remains consistently strong across contrasting field conditions.

3.3. Post-Hoc Comparison of Variable Fumigation Rates

After accounting for field- and flight-level effects, RSF-derived canopy risk did not differ meaningfully among fumigant application rates. Within each field, normalized RSF risk scores were compared among available fumigation rates (280, 336, and 392 kg Pic-Clor 60/ha) using balanced subsamples and linear models that controlled for flight date (Table 4). Across all within-field contrasts, estimated treatment effects were small in magnitude on the 0–1 normalized risk scale, and 95% confidence intervals overlapped zero in all cases. Differences among fumigation rates were substantially smaller than field-level differences in canopy risk observed across the season. Empirical cumulative distribution functions likewise showed highly overlapping risk distributions within fields. Taken together, these results indicate no detectable association between pre-plant fumigation rate and RSF-estimated canopy decline risk in this observational setting. Given the non-randomized block design and absence of replication, these findings should be interpreted as descriptive associations rather than causal estimates of treatment efficacy.

Table 4. Within-field contrasts in normalized RSF-derived canopy risk among fumigant application rates. Effects (Δ) represent differences in mean normalized canopy risk estimated using linear models with flight-clustered standard errors across four survey flights per field. Confidence intervals are 95% intervals from the primary model. *n* denotes the number of plant-level monitoring units included in each balanced comparison.

Field	Treatment (kg/ha)	Δ Normalized Risk	95% CI	*n*
1	392 vs. 280	0.021	−0.004, 0.045	32,816
2	392 vs. 336	−0.003	−0.008, 0.003	27,648
3	336 vs. 280	0.000	−0.001, 0.002	59,976
3	392 vs. 280	0.000	−0.002, 0.001	59,976
3	392 vs. 336	−0.001	−0.002, 0.000	60,144

4. Discussion

This study demonstrates that repeated UAV multispectral observations, when integrated within a plant-level survival modeling framework, can characterize the onset and spatial progression of canopy decline in commercial strawberry systems. Across three fields spanning contrasting canopy decline regimes, Random Survival Forest (RSF) models consistently ranked plants by time-to-decline risk (overall C-index 0.88–0.95). Risk surfaces reflected both the intensity and spatial organization of canopy stress, distinguishing widespread consolidation (Field 1) from diffuse low-intensity risk (Field 2) and localized persistence (Field 3). Modeling canopy decline as a time-to-event process allows relative risk to be quantified under heterogeneous field conditions where static classification approaches are often unstable.

Compared to conventional field scouting, single-date vegetation indices, or end-of-season yield assessments, the RSF framework provides a time-aware, plant-level representation of canopy decline that integrates spatial structure and temporal progression. In Field 1, where canopy decline intensified and became spatially coordinated, classification performance peaked during periods of coherent spatial expansion. In Fields 2 and 3, where decline incidence was lower and spatially heterogeneous, binary classification performance varied across flights, reflecting differences in event prevalence and spatial organization.

The canopy stress patterns detected in this study are consistent with previous remote sensing research showing that multispectral vegetation indices respond sensitively to plant disease–related physiological changes. UAV-based multispectral imagery has been used to detect banana Fusarium wilt [32], vascular pathogen symptoms in tree crops [33], and cotton root rot [34]. NDRE and red–green indices have also demonstrated responsiveness to early canopy stress in soybean [35], maize [36], and strawberry leaf spot [20]. The spectral dynamics observed in this study (i.e., declining NDRE and increasing Redness Index values) are consistent with reduced chlorophyll content, canopy thinning, and early senescence. In systems affected by *Macrophomina phaseolina*, crown and root rot can impair water and nutrient uptake before overt wilting, producing canopy-level stress responses that align with these spectral signatures. Although pathogen presence was not confirmed at the individual-plant level, the spectral dynamics observed here are consistent with known physiological responses to root and vascular impairment.

Survival-based ranking performance remained stable across all three fields. Overall concordance indices (0.88–0.95) fall within ranges generally interpreted as strong discriminatory ability in survival modeling applications [37]. Random Survival Forest models have demonstrated strong predictive performance in ecological time-to-event contexts, including forest harvest dynamics and mortality modeling [38]. Although performance metrics vary across studies (e.g., C-index, AUC, or Brier score), these applications collectively indicate that survival-based machine learning methods are well-suited for modeling complex biological time-to-event processes. While RSF has been widely studied in medical and ecological survival analysis [39,40], explicit plant-level time-to-event modeling of UAV-derived canopy stress trajectories in commercial crop systems remains limited. The contribution of the present study lies not in proposing a new survival algorithm, but in adapting survival-based machine learning to repeated high-resolution canopy observations to model decline progression under operational agricultural conditions.

These observations also highlight a limitation of many UAV-based crop stress studies, which often utilize single-date classification or foliar symptom detection frameworks. In contrast, the present study embeds stress-sensitive spectral indices within a plant-level time-to-event survival modeling structure. By modeling canopy decline as a temporal hazard process rather than a static classification outcome, the approach extends prior index-based disease detection research toward dynamic risk prediction under heterogeneous field conditions. Explicit plant-level time-to-event modeling of UAV-derived canopy stress trajectories in commercial crop systems remains limited. This perspective shifts UAV-based canopy monitoring from static stress detection toward explicit modeling of decline progression through time.

One of the key insights emerging from this framework is the importance of spatial organization in canopy decline dynamics. Across all three study fields, risk maps revealed coherent zones of elevated canopy stress even under low-prevalence conditions. The ability to resolve plant-level spatial structure highlights the advantage of high-resolution UAV monitoring over field-averaged metrics and supports management strategies that target localized stress zones rather than entire fields.

For soilborne pathogens that invade the root and vascular system, effective in-season chemical control options are limited once infection has occurred. In this context, early identification of high-risk zones may still support stress-mitigating practices such as optimized irrigation management, targeted scouting, or localized management adjustments. The practical value of early risk identification lies less in curative intervention than in enabling informed, site-specific management decisions during the production season.

Post-hoc comparisons among variable fumigant application rates revealed no detectable association between fumigation intensity and RSF-estimated canopy risk in this observational layout. Effect sizes were small, and confidence intervals overlapped zero, consistent with the non-randomized treatment arrangement and lack of sufficient block replication. These findings should be interpreted as descriptive associations rather than causal estimates of treatment efficacy. Although no clear relationship between application rate and modeled canopy risk was observed during the growing season, formal inference regarding rate sufficiency requires replicated experimental designs. Nevertheless, UAV-derived risk maps provide spatial context that may inform post-season management decisions, including fumigation planning, field selection, and input allocation for subsequent production cycles.

Although this study evaluated strawberry systems specifically, the framework is not pathogen-specific. Because it models canopy decline as a temporal process using general stress-related spectral responses, the approach may be adaptable to other high-value crops where heterogeneous canopy stress is driven by soilborne disease, water limitation, or localized management constraints. However, transferability across crops and environments requires empirical validation.

A related methodological question is whether a single pooled RSF model could be trained across multiple fields rather than fitting field-specific models. In the present study, models were fit independently to account for differences in baseline canopy decline intensity, soil conditions, and management history. Although parameter estimates are field-specific, the consistent survival ranking performance observed across contrasting disease regimes suggests that the underlying modeling structure is robust. In this context, generalizability pertains to the analytical framework and feature construction pipeline rather than to the direct transfer of fitted model parameters. Future work could evaluate hierarchical or pooled survival models that share information across fields while allowing field-level baseline hazards to vary.

Several limitations should be acknowledged. Pathogen presence was not confirmed at the individual-plant level, and spectral responses to disease may overlap with abiotic stressors. The analysis was conducted over a single growing season, and NDRE and RI thresholds were empirically defined rather than physiologically calibrated. Future research should evaluate adaptive or relative thresholding strategies, such as percentile-based or distribution-based classification within field–date combinations, to enhance transferability across sensors, cultivars, and environmental conditions. Future work should also focus on multi-season validation, integration of environmental covariates, and evaluation across additional cultivars and disease pressures.

5. Conclusions

This study demonstrates that integrating plant-level UAV multispectral observations with survival modeling provides a structured framework for quantifying and mapping spatiotemporal canopy decline risk in commercial strawberry systems. By modeling canopy decline as a time-to-event process, the approach advances beyond static vegetation index mapping toward explicit representation of decline progression under heterogeneous field conditions.

Across contrasting canopy stress regimes, the framework consistently ranked plants by relative risk and generated spatially coherent risk surfaces that aligned with observed canopy dynamics. While further multi-season validation and pathogen-level confirmation are needed, this survival-based modeling strategy offers a scalable foundation for spatially informed monitoring and decision support in high-value cropping systems.

Author Contributions: J.R.D. conceived and designed the analytical framework for the study, developed the modeling approach, performed the formal analysis, and prepared the original draft of the manuscript. C.A.G. conducted the UAV surveys, performed image processing and data prepa-

ration, and assisted with technical documentation for the manuscript. O.D. coordinated field site establishment, liaised with growers, and provided site-specific background information, and assisted with review of the manuscript. A.J.P. provided feedback on manuscript drafts and contributed to discussions on methodological development. F.S.M. contributed to the initial motivation and conceptual design for the study and assisted with review of the manuscript. F.N.M. developed and led the broader research project, provided supervision and critical review of the manuscript, and acquired funding. All authors have read and agreed to the published version of the manuscript.

Funding: This research was supported by the Area-Wide Pest Management Grant Program Project Award No. 58-2038-9-017 and Project Award No. 58-2038-2-029 from the U.S. Department of Agriculture's National Institute of Food and Agriculture. Contributions by F.S.M. were supported by the NASA Earth Action Agriculture Program Element. Contributions by A.J.P. were supported in part by NASA's Western Water Action Office.

Data Availability Statement: The data supporting the findings of this study, including UAV imagery and derived plant-level metrics, as well as the analysis scripts, are available from the corresponding author upon reasonable request due to data volume and grower confidentiality considerations.

Acknowledgments: The authors thank collaborating growers for providing access to field sites and logistical support during data collection, and acknowledge technical assistance provided by project staff during UAV data collection. This work was conducted in collaboration with the U.S. Department of Agriculture, Agricultural Research Service (USDA-ARS), Salinas, CA, USA.

Conflicts of Interest: The authors declare no conflict of interest. The funders had no role in the design of the study; in the collection, analyses, or interpretation of data; in the writing of the manuscript; or in the decision to publish the results.

References

1. Simpson, D. The Economic Importance of Strawberry Crops. In *The Genomes of Rosaceous Berries and Their Wild Relatives*; Hytönen, T., Graham, J., Harrison, R., Eds.; Compendium of Plant Genomes; Springer: Cham, Switzerland, 2018. [CrossRef]
2. California Strawberry Commission. *CSC Benefits Report 2018–2023*; California Strawberry Commission: Watsonville, CA, USA, 2024. Available online: https://www.californiastrawberries.com/wp-content/uploads/2024/08/CSC-Benefits-Report-2018-2023-FINAL.pdf (accessed on 16 March 2026).
3. Holmes, G.J. The California Strawberry Industry: Current Trends and Future Prospects. *Int. J. Fruit Sci.* **2024**, *24*, 115–129. [CrossRef]
4. California Department of Food and Agriculture. *California Agricultural Statistics Review 2022–2023*; California Department of Food and Agriculture: Sacramento, CA, USA, 2023. Available online: https://www.cdfa.ca.gov/Statistics/PDFs/2022-2023_california_agricultural_statistics_review.pdf (accessed on 16 March 2026).
5. Chamorro, M.; Miranda, L.; Domínguez, P.; Medina, J.J.; Soria, C.; Romero, F.; López-Aranda, J.M.; De los Santos, B. Evaluation of Biosolarization for the Control of Charcoal Rot Disease (*Macrophomina phaseolina*) in Strawberry. *Crop Prot.* **2015**, *67*, 279–286. [CrossRef]
6. Alizadeh, M.; Khodadadi Manesh, S.; Fathi, P.; Karimi, H.; Tavakol Noorabadi, M.; Roshanroo, M.; Karimzadeh, S.; Doni, F.; Rahimi-Soujeh, Z.; Ghaleh, M.K.; et al. Biology and Host Ranges of the Plant Pathogenic Fungus *Macrophomina phaseolina*: A Comprehensive Review. *J. Crop Health* **2025**, *77*, 50. [CrossRef]
7. Holmes, G.; Mansouripour, S.; Hewavitharana, S. Strawberries at the Crossroads: Management of Soilborne Diseases in California without Methyl Bromide. *Phytopathology* **2020**, *110*, 956–968. [CrossRef]
8. Koike, S.T.; Arias, R.S.; Hogan, C.S.; Martin, F.N.; Gordon, T.R. Status of Macrophomina phaseolina on Strawberry in California and Preliminary Characterization of the Pathogen. *Int. J. Fruit Sci.* **2016**, *16*, 148–159. [CrossRef]
9. California Department of Pesticide Regulation. *DPR Releases First Phase of State-Funded Fumigant Alternatives Study Focused on 1,3-D and Chloropicrin*; Press Release; California Department of Pesticide Regulation: Sacramento, CA, USA, 2025. Available online: https://cdpr.ca.gov/2025/03/13/dpr-releases-first-phase-of-state-funded-fumigant-alternatives-study-focused-on-13-d-and-chloropicrin/ (accessed on 16 March 2026).
10. Nutter, F. W. The Role of Plant Disease Epidemiology in Developing Successful Integrated Disease Management Programs. In *General Concepts in Integrated Pest and Disease Management*; Ciancio, A., Mukerji, K.G., Eds.; Springer: Berlin/Heidelberg, Germany, 2007; Volume 1, pp. 203–226. [CrossRef]
11. Oerke, E.C. Remote Sensing of Diseases. *Annu. Rev. Phytopathol.* **2020**, *58*, 225–252. [CrossRef]

12. Gogoi, N.K.; Deka, B.; Bora, L.C. Remote Sensing and Its Use in Detection and Monitoring of Plant Diseases: A Review. *Agric. Rev.* **2018**, *39*, 307–313. [CrossRef]
13. Mahlein, A.K.; Rumpf, T.; Welke, P.; Dehne, H.W.; Plümer, L.; Steiner, U.; Oerke, E.C. Development of Spectral Indices for Detecting and Identifying Plant Diseases. *Remote Sens. Environ.* **2013**, *128*, 21–30. [CrossRef]
14. Calderón, R.; Navas-Cortés, J.A.; Lucena, C.; Zarco-Tejada, P.J. High-Resolution Airborne Hyperspectral and Thermal Imagery for Early Detection of Verticillium Wilt of Olive Using Fluorescence, Temperature and Narrow-Band Spectral Indices. *Remote Sens. Environ.* **2013**, *139*, 231–245. [CrossRef]
15. Kouadio, L.; El Jarroudi, M.; Belabess, Z.; Laasli, S.E.; Roni, M.Z.K.; Amine, I.D.I.; Mokhtari, N.; Mokrini, F.; Junk, J.; Lahlali, R. A Review on UAV-Based Applications for Plant Disease Detection and Monitoring. *Remote Sens.* **2023**, *15*, 4273. [CrossRef]
16. Chakhvashvili, E.; Machwitz, M.; Antala, M.; Rozenstein, O.; Prikaziuk, E.; Schlerf, M.; Naethe, P.; Wan, Q.; Komárek, J.; Klouek, T.; et al. Crop Stress Detection from UAVs: Best Practices and Lessons Learned for Exploiting Sensor Synergies. *Precis. Agric.* **2024**, *25*, 2614–2642. [CrossRef]
17. Mahlein, A.K. Plant Disease Detection by Imaging Sensors: Parallels and Specific Demands for Precision Agriculture and Plant Phenotyping. *Plant Dis.* **2016**, *100*, 241–251. [CrossRef] [PubMed]
18. Zarco-Tejada, P.J.; González-Dugo, M.V.; Fereres, E. Seasonal Stability of Chlorophyll Fluorescence Quantified from Airborne Hyperspectral Imagery as an Indicator of Net Photosynthesis in the Context of Precision Agriculture. *Remote Sens. Environ.* **2016**, *179*, 89–103. [CrossRef]
19. Wu, G.; Fang, Y.; Jiang, Q.; Cui, M.; Li, N.; Ou, Y.; Diao, Z.; Zhang, B. Early Identification of Strawberry Leaf Diseases Utilizing Hyperspectral Imaging Combined with Spectral Features, Multiple Vegetation Indices and Textural Features. *Comput. Electron. Agric.* **2023**, *204*, 107553. [CrossRef]
20. Rojas, A.E.F.; González, L.C.; Carrillo, D.A.P. Firma Espectral de Peca de la Hoja (*Mycosphaerella fragariae* (Tul.)) en Plantas de Fresa (*Fragaria* × *ananassa* Duch) Relacionada a NDVI y NDRE. *Ing. Cienc.* **2023**, *19*, 4. [CrossRef]
21. Mahmud, M.S.; Zaman, Q.U.; Esau, T.J.; Chang, Y.K.; Price, G.W.; Prithiviraj, B. Real-Time Detection of Strawberry Powdery Mildew Disease Using a Mobile Machine Vision System. *Agronomy* **2020**, *10*, 1027. [CrossRef]
22. Chang, Y.K.; Mahmud, M.S.; Shin, J.; Nguyen-Quang, T.; Price, G.W.; Prithiviraj, B. Comparison of Image Texture Based Supervised Learning Classifiers for Strawberry Powdery Mildew Detection. *AgriEngineering* **2019**, *1*, 434–452. [CrossRef]
23. Mahbub, J.; Bhandari, S.; Raheja, A.; Gonzalez, C. Machine Learning Models to Detect Strawberry Plant Health from UAVs for Real-Time Applications. In *Proceedings of the Autonomous Air and Ground Sensing Systems for Agricultural Optimization and Phenotyping X, Orlando, FL, USA, 14–16 April*; SPIE: Bellingham, WA, USA, 2025; Volume 13475, pp. 213–226. [CrossRef]
24. Bzdok, D.; Altman, N.; Krzywinski, M. Statistics versus Machine Learning. *Nat. Methods* **2018**, *15*, 233–234. [CrossRef]
25. Zheng, C.; Abd-Elrahman, A.; Whitaker, V. Remote Sensing and Machine Learning in Crop Phenotyping and Management, with an Emphasis on Applications in Strawberry Farming. *Remote Sens.* **2021**, *13*, 531. [CrossRef]
26. Ishwaran, H.; Kogalur, U.B.; Blackstone, E.H.; Lauer, M.S. Random Survival Forests. *Ann. Appl. Stat.* **2008**, *2*, 841–860. [CrossRef]
27. Rumpf, T.; Mahlein, A.K.; Steiner, U.; Oerke, E.C.; Dehne, H.W.; Plümer, L. Early Detection and Classification of Plant Diseases with Support Vector Machines Based on Hyperspectral Reflectance. *Comput. Electron. Agric.* **2010**, *74*, 91–99. [CrossRef]
28. Pourazar, H.; Samadzadegan, F.; Dadrass Javan, F. Aerial multispectral imagery for plant disease detection: Radiometric calibration necessity assessment. *Eur. J. Remote Sens.* **2019**, *52*, 17–31. [CrossRef]
29. Kreigler, F.J.; Malila, W.A.; Nalepka, R.F.; Richardson, W. Preprocessing Transformations and Their Effects on Multispectral Recognition. In Proceedings of the Proceedings of the Sixth International Symposium on Remote Sensing of Environment, Ann Arbor, MI, USA, 13–16 October 1969; Volume 1, pp. 97–131.
30. Gitelson, A.; Merzlyak, M.N. Quantitative Estimation of Chlorophyll-a Using Reflectance Spectra: Experiments with Autumn Chestnut and Maple Leaves. *J. Photochem. Photobiol.* **1994**, *13*, 247–252. [CrossRef]
31. Hunt, E.R.J.; Cavigelli, M.; Daughtry, C.S.T.; McMurtrey, J.E., III; Walthall, C.L. Evaluation of Digital Photography from Model Aircraft for Remote Sensing of Crop Biomass and Nitrogen Status. *Precis. Agric.* **2005**, *6*, 359–378. [CrossRef]
32. Zhang, S.; Li, X.; Ba, Y.; Lyu, X.; Zhang, M.; Li, M. Banana Fusarium wilt disease detection by supervised and unsupervised methods from UAV-based multispectral imagery. *Remote Sens.* **2022**, *14*, 1231. [CrossRef]
33. Poblete, T.; Navas-Cortés, J.A.; Hornero, A.; Camino, C.; Calderón, R.; Hernández-Clemente, R.; Zarco-Tejada, P.J. Detection of symptoms induced by vascular plant pathogens in tree crops using high-resolution satellite data: Modelling and assessment with airborne hyperspectral imagery. *Remote Sens. Environ.* **2023**, *295*, 113698. [CrossRef]
34. Yang, C.; Fernandez, C.J.; Everitt, J.H. Comparison of airborne multispectral and hyperspectral imagery for mapping cotton root rot. In Proceedings of the ASABE Annual International Meeting, Reno, NV, USA, 21–24 June 2009; p. 1. [CrossRef]
35. Brodbeck, C.; Sikora, E.; Delaney, D.; Pate, G.; Johnson, J. Using unmanned aircraft systems for early detection of soybean diseases. *Adv. Anim. Biosci.* **2017**, *8*, 802–806. [CrossRef]
36. Radócz, L.; Juhász, C.; Tamás, A.; Illés, Á.; Ragán, P.; Radócz, L. Multispectral UAV-Based Disease Identification Using Vegetation Indices for Maize Hybrids. *Agriculture* **2024**, *14*, 2002. [CrossRef]

37. Uno, H.; Cai, T.; Pencina, M.J.; D'Agostino, R.B.; Wei, L.J. On the C-statistics for evaluating overall adequacy of risk prediction procedures with censored survival data. *Stat. Med.* **2011**, *30*, 1105–1117. [CrossRef] [PubMed]
38. Senevirathne, D.M.; Yang, S.I.; Brandeis, C.; Hodges, D.G. Predicting time-to-harvest in mixed-species forests using a random survival forest algorithm. *For. Ecosyst.* **2024**, *11*, 100236. [CrossRef]
39. Qiu, X.; Gao, J.; Yang, J.; Hu, J.; Hu, W.; Kong, L.; Lu, J.J. A Comparison Study of Machine Learning (Random Survival Forest) and Classic Statistic (Cox Proportional Hazards) for Predicting Progression in High-Grade Glioma After Proton and Carbon Ion Radiotherapy. *Front. Oncol.* **2020**, *10*, 551420. [CrossRef] [PubMed]
40. Cutler, D.R.; Edwards, T.C.; Beard, K.H.; Cutler, A.; Hess, K.T.; Gibson, J.; Lawler, J.J. Random Forests for Classification in Ecology. *Ecology* **2007**, *88*, 2783–2792. [CrossRef] [PubMed]